Microsystem Technologies
https://doi.org/10.1007/s00542-020-05031-0

TECHNICAL PAPER

# Multiphysics simulation of hypersensitive microbolometer sensor using vanadium dioxide and air suspension for millimeter wave imaging

Shangyi Chen[1,2] · Mark Lust[1] · Nima Ghalichechian[1]

Received: 23 August 2020 / Accepted: 3 September 2020


## Abstract

A highly sensitive uncooled antenna-coupled microbolometer for millimeter wave (mmW) imaging is reported in this paper. Vanadium dioxide ($VO_2$) phase-change material is utilized in our design to exploit its non-linear change in electrical resistivity. The proposed microbolometer takes advantage of the large thermal coefficient of resistance (TCR) of $VO_2$ at the non-linear region. The thermal resistance of the device is significantly improved by micro-electro-mechanical systems (MEMS) techniques to suspend the device above the substrate, compared with non-suspended microbolometers. Unlike semiconductor-based sensors that are characterized by capacitive roll-off limitations, the proposed antenna-coupled sensor has an inherently high operating frequency and wide bandwidth suitable for mmW imagers. The finite element method is employed to analyze the electrothermal and electromagnetic performance of the device. The frequency range of operation is 65–85 GHz, and the realized gain at broadside is $> 1.0$ dB. Simulation results indicate a high responsivity of $1.72 \times 10^3$ V/W and a low noise equivalent power (NEP) of 33 pW/$\sqrt{\text{Hz}}$. The enhanced device sensitivity is primarily the result of the sharp change in $VO_2$'s electrical resistivity and is assisted by air suspension using MEMS microfabrication processes. In this work, for the first time, using multiphysics modeling we demonstrate exploitation of $VO_2$'s non-linear behavior in enhancing the sensitivity of a conventional microbolometer. Based on the findings of this study, a pixilated array of the proposed sensors will enable the realization of a highly sensitive mmW camera for a variety of sensing applications.

## 1 Introduction

As compared to the microwave band, the millimeter wave (mmW) band contains shorter wavelengths and is generally defined by frequencies between 30 and 300 GHz. The radiation in the mmW domain penetrates certain obstacles, fog, and clothing, which together with better spatial resolution than lower frequencies, makes it attractive for non-destructive evaluation (Ghasr et al. 2013), biomedical screening (Joung et al. 2004), defense (Schuetz et al. 2007), and surveillance applications (Appleby and Anderton 2007). In all of these sensing and measurement applications, a real-time mmW imager is necessary. Further, given the importance of the blackbody radiation measurement from an object, a high detection sensitivity of the imager is desired. The majority of the detection schemes developed thus far includes the zero-bias Schottky diodes (Hesler and Crowe 2007; Yang et al. 2015), Golay cells (Denison et al. 2009), and microbolometers (Miller et al. 2004; Neikirk et al. 1984; Tiwari et al. 2015; Yoneoka et al. 2011). Of these, the microbolometers are perhaps the most useful given the wideband operation, low cost, and monolithic fabrication with read-out integrated circuits (ROIC). Improving the responsivity of a microbolometer is possible through the use of non-linear materials with a large thermal coefficient of resistance (TCR). Traditionally, materials with a moderate TCR ($\sim 0.2\%$/K) and with electrical resistances that change linearly with temperature are utilized. Such examples include titanium (Tiwari et al. 2015), niobium (Miller et al. 2004), platinum (Yoneoka et al. 2011), and bismuth (Neikirk et al. 1984). Vanadium oxide

✉ Shangyi Chen
chen.6642@osu.edu

[1] ElectroScience Laboratory, Department of Electrical and Computer Engineering, The Ohio State University, Columbus, OH 43212, USA

[2] Department of Mechanical and Aerospace Engineering, The Ohio State University, Columbus, OH 43212, USA

Published online: 12 September 2020

($VO_x$) with a larger TCR in the dielectric phase compared to most metals is also commonly used. Specifically, $VO_x$ microbolometers were reported operating in both infrared (IR) and mmW bands with a measured TCR of 6.5%/K (Wang et al. 2013) and 4.8%/K (Son et al. 2013), respectively. Phase-change materials (PCM) such as vanadium dioxide ($VO_2$) have also been utilized in the IR region. $VO_2$ has a metal–insulator transition (MIT), which causes a sharp, non-linear change in electrical resistivity by several orders of magnitude. However, most of the IR sensors have only demonstrated a degree of functionality in the dielectric phase of $VO_2$ (Chen et al. 2001; Chen and Yi 2005). Although microbolometers with a large TCR in the MIT region of $VO_2$ were previously implemented, no improvement was observed in performance (De Almeida et al. 2004; Reintsema et al. 1999; Zerov et al. 1999). In one example, the absence of responsivity (108 V/W) was attributed to the inferior quality of the deposited film (Reintsema et al. 1999). However, a single pulse excitation for an IR microbolometer with a heater design (Zerov et al. 1999), together with theoretical verification was subsequently used to improve this responsivity (De Almeida et al. 2004). While some theoretical studies (Neto et al. 2008) suggest improvement to the responsivity of $VO_2$ microbolometers operating within the MIT region, sensors based upon this responsivity have yet to be developed.

In this paper, we present for the first time a highly sensitive ($> 10^3$ V/W responsivity) $VO_2$ mmW microbolometer developed through a biasing of the PCM sensor in the phase transition region. The overall performance of the proposed microbolometer (Chen et al. 2018, 2019) is further enhanced via micro-electro-mechanical systems (MEMS) processing to suspend the sensing element. In our group, we have developed a deposition technique for $VO_2$ thin films on silicon (Si) and sapphire substrates that exhibit $1.46 \times 10^4$ and $9.76 \times 10^4$ times change in resistivity, respectively (Lust et al. 2020). $VO_2$ thin films are presented to have high resistivity contrast on Si substrates through adding crystallized alumina ($Al_2O_3$) buffer layers. The deposition technique and $VO_2$'s behaviors are employed in the design of the proposed microbolometer. Experimental data served to numerically evaluate the TCR of the $VO_2$ thin film, and multiphysics simulation using the finite element method (FEM) and analytical studies were used to analyze the microbolometer. The goal of this study was to illustrate the concept of a novel uncooled antenna-coupled microbolometer with high sensitivity, low noise, wideband operation, and fast transient response. The sensor can be expanded into an array for implementation in an mmW imaging system at room temperature.

## 2 Design

### 2.1 Microbolometer structure

A microbolometer is a well-established device with an electrical resistance that changes with the temperature due to radiation absorption. The resistance change can be measured and recorded by a ROIC. The conceptual design of the antenna-coupled sensor is shown in Fig. 1. Each $VO_2$ microbolometer pixel is coupled and matched to a wideband dipole antenna (with a ground plane) and ROIC. The schematics of cross-section and top view are shown in Fig. 2. The $VO_2$ sensor is suspended from the Si substrate by employing an $Al_2O_3$ buffer layer. This chosen buffer layer has several functions: it facilitates lattice-matched growth for the $VO_2$ thin film to increase the electrical resistivity contrast in the phase change; its well-defined atomic layer deposition process on the Si substrate is important for the monolithic integration of sensors; and its use as a membrane for suspending the $VO_2$ sensor yields a robust structure. Compared to traditional on-substrate designs, this MEMS suspension significantly improves the thermal resistance (isolation) of the microbolometer.

### 2.2 Microbolometer physics

To obtain the optimal performance of the microbolometer, the design parameters need to be analyzed. Key figures of merit used to characterize the performance of a microbolometer are TCR, responsivity, and noise equivalent power (NEP). TCR quantifies the temperature dependence of resistance and is given by:

$$\alpha = \frac{dR}{RdT} \quad (1)$$

where $R$ is the electrical resistance of the sensor and $T$ is the average temperature of the microbolometer. Responsivity is defined as the ratio of the obtained output voltage per unit of input radiation power:

$$\mathfrak{R} = \frac{\Delta\mathfrak{V}}{\Delta\mathfrak{P}} \quad (2)$$

and is also expressed as:

$$\mathfrak{R} = \mathfrak{I}_{\mathfrak{b}}\mathfrak{R}\alpha\left|\frac{\mathfrak{R}_{\mathfrak{th}}}{+\mathfrak{j}\pi\mathfrak{f}\tau}\right| \quad (3)$$

where $I_b$ is the bias current, $R_{th}$ is the total thermal resistance, $\tau$ is the transient response, and $f$ is the radiation modulation frequency. NEP is a function of responsivity and noise voltage, expressed as:

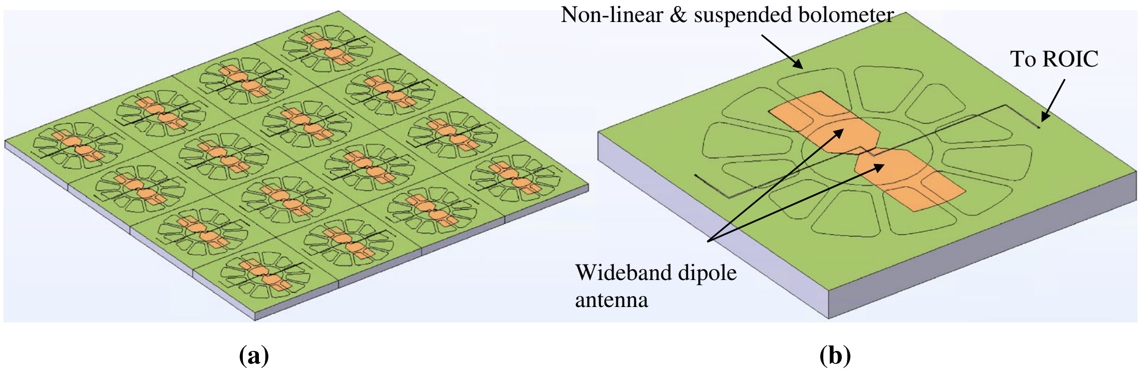


**Fig. 1** Conceptual design of **a** 4 × 4 array of an mmW imager and **b** a unit cell, or pixel, composed of a suspended non-linear PCM sensor coupled to an mmW antenna and ROIC

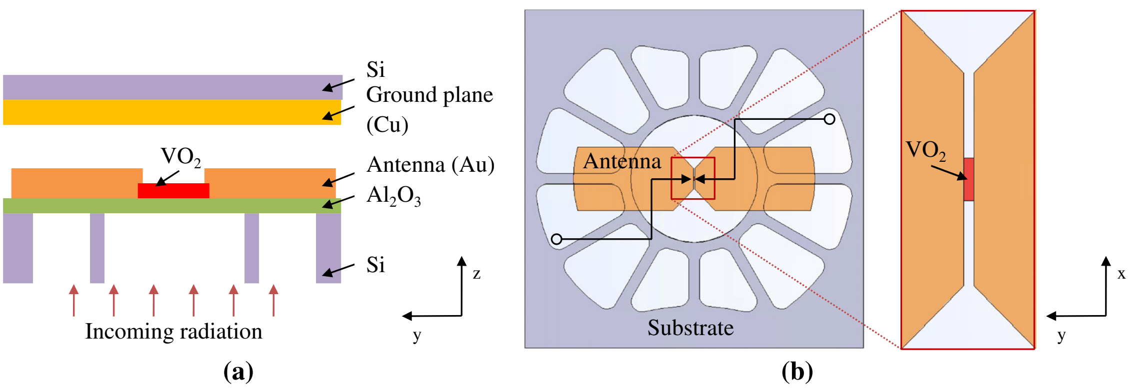


**Fig. 2** **a** Cross-section schematic and **b** top-view of the PCM microbolometer (without the $Al_2O_3$ layer)

$$NEP = \frac{S_n}{\Re} \tag{4}$$

where $S_n$ is the total noise from microbolometer that is a combination of several uncorrelated sources: Johnson, Phonon, and *1/f* noise defined as (Yang and Rebeiz 2015):

$$S_n^2 = S_{Johnson}^2 + S_{phonon}^2 + S_{1/f}^2 \tag{5}$$

$$S_{Johnson}^2 = 4k_B TR \tag{6}$$

$$S_{phonon}^2 = 4k_B T^2 \frac{\Re^2}{|R_{th}|} \tag{7}$$

$$S_{1/f}^2 \propto I_b^2 R \frac{1}{f^n} \tag{8}$$

where $k_B$ is Boltzmann's constant, and Eq. (8) is an experimental relation with $n \sim 1$.

As shown in Eq. (3), the responsivity is directly proportional to the TCR. For this reason, we propose to use a non-linear material with a high TCR value. $VO_2$ is particularly attractive due to its sharp electrical resistance change in the MIT region, a relatively low transition temperature (68 °C), small hysteresis (4 °C) (Lust et al. 2020), and a fast intrinsic response time (De Almeida et al. 2004). In this study, the abrupt change in the resistivity of $VO_2$ film is exploited by biasing the device at the phase change cliff ($\sim$ 72 °C). A small temperature increase caused by radiation absorption by the wideband antenna in 65–85 GHz band, will translate to significant change in resistivity. This characterization of temperature dependence of resistance is quantified by TCR. In an experimental result, our 107-nm-thick $VO_2$ films on 23-nm-thick annealed $Al_2O_3$ buffer layer on Si yielded a $> 1 \times 10^4$ resistivity change between the dielectric and conducting states. The measured resistivity (logarithmic scale) and the calculated TCR are shown in Fig. 3. To calculate TCR, the logarithmic value of discrete resistivity (experimental results) is fitted to a shape preserving function known as the piecewise cubic Hermite interpolating polynomial. A five-point numerical differentiation is then applied to obtain the derivative of the fitted function. Table 1 lists a comparison of TCR values of our $VO_2$ films in the MIT region with values for commonly used bolometer materials. The absolute TCR of $VO_2$, which reaches 171%/K in the MIT region, is $\sim 10^3$ times larger than the value of general metallic materials. Thus, the responsivity of the proposed uncooled microbolometer is greatly improved.

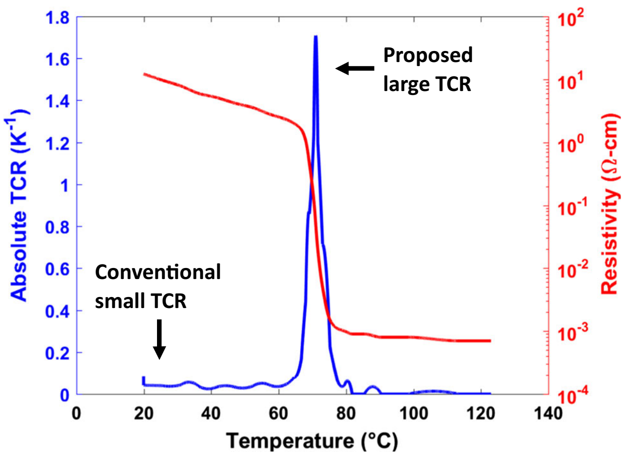


**Fig. 3** Measured resistivity (right axis) and calculated TCR (left axis) for our 107-nm-thick $VO_2$ films

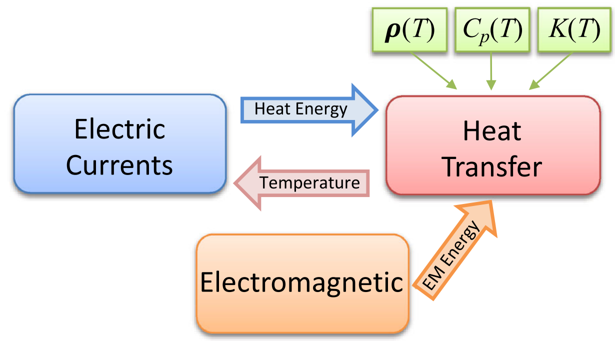


**Fig. 4** Flow chart of the multiphysics simulation for the PCM sensor

## 3 Simulation and discussion

A finite element analysis using COMSOL was next conducted to model the multiphysics behavior and provide an accurate prediction of the microbolometer performance. Specifically, the challenges in the simulation include $VO_2$'s sharp resistance change near the transition region resulting in a non-linear unstable problem; the mesh generation for the multi-scale geometric model; and the appropriate partial differential equation (PDE) solvers for this highly dynamic problem. To overcome these issues, we first studied the reasonable boundary conditions (BCs) to mimic the non-linear unstable behaviors. After comparing different BCs, the normal current density BC was then employed to create stable heat source. Secondly, the meshes were generated by different methods including swept mesh and free tetrahedral for each component to significantly reduce the number of the degree of freedom. Moreover, the elements were grown from the small component ($VO_2$) to the large one (air) to guarantee the conforming mesh. Finally, the Heat Transfer and AC/DC modules were coupled and solved using a time-dependent solver. The flow chart of the multiphysics simulation is illustrated in Fig. 4. When applying a biased current to the sensor, Joule heating is used to couple the generated heat energy to the Heat Transfer module. The temperature is coupled back to the AC/DC module to account for the change in the electrical conductivity. Therefore, we can obtain the temperature distribution across the sensor as well as the dynamic response. The characteristics of the antenna were demonstrated using the RF module. The received power by the antenna were obtained with background radiation and were then utilized to calculate the temperature change and output voltage change. Results from the simulation are used to estimate the sensitivity and validate the properties of the proposed suspended architecture.

### 3.1 Electrothermal behavior

In order to impedance-match the bolometer sensor at ~ 200 Ω with the antenna, the dimensions of $VO_2$ sensor were set at 10 μm × 40 μm × 0.107 μm based on the known resistivity of our $VO_2$ thin films. The initial ambient temperature of both the sensor and air was set to 293.15 K. Since $VO_2$ has a first-order phase transition, the latent heat during the transition (Berglund and Guggenheim 1969; Kawakubo and Nakagawa 1964) was used in the material settings. The temperature dependent conductivity of $VO_2$ was also used (Ordonez-Miranda et al. 2018). With the same bias current, the temperature profile of both the on-substrate and suspended designs are shown in Fig. 5. The x-axis represents the vertical position of the sensor, from

**Table 1** TCR comparison for the different materials

| | Material | TCR (K$^{-1}$) |
|---|---|---|
| This sensor | $VO_2$ | − 171% (Phase transition region) |
| (Chen and Yi 2005) | $VO_2$ | − 2% (Semiconductor phase) |
| (Wang et al. 2013) | $VO_x$ | − 6.5% (Semiconductor phase) |
| (Son et al. 2013) | $VO_x$ | − 4.8% (Semiconductor phase) |
| (Neikirk et al. 1984) | Bismuth | 0.3% |
| (Miller et al. 2004) | Niobium | 0.214% |
| (Yoneoka et al. 2011) | Platinum | 0.14% (Average) |
| (Tiwari et al. 2015) | Titanium | 0.15% |

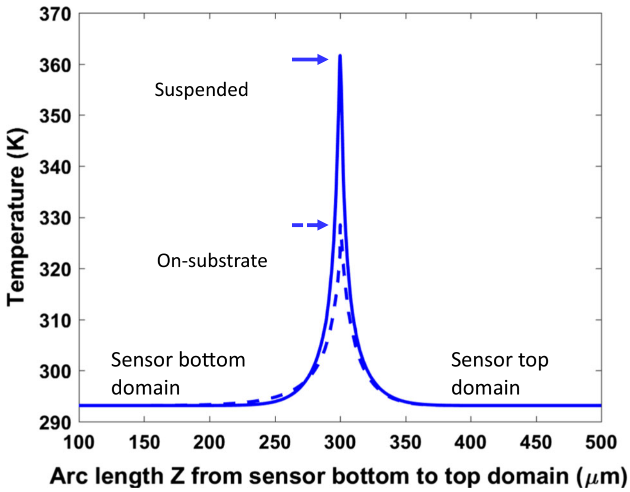


**Fig. 5** Temperature profile across the sensor for the on-substrate and suspended designs

the bottom through the top domain of the device. The y-axis indicates the temperature of the different positions. The maximum temperature of the suspended sensor is 30 K larger than that of the on-substrate design. Figure 6 shows the 2D cross-sectional temperature distribution of these two designs. As illustrated in Fig. 6, no obvious temperature change is evident underneath the sensor surface in the 2D cross-sectional temperature distribution for the on-substrate design, indicating a dissipation of most of the heat into the substrate. However, a significant temperature contrast of the sensor surface with the outside air domain is evident as depicted in the suspension design. This indicates a larger thermal resistance (isolation) by suspension of the PCM. The thermal resistance of the sensor is estimated by both the input power and the corresponding temperature change of the sensor. The thermal resistance increases from 77 K/W when on the substrate, to $6 \times 10^3$ K/W when fully suspended in air. The dynamic temperature response of the suspended microbolometer with a 1.43 mA pulsed current bias is shown in Fig. 7. The steady state temperature is 345.53 K with a 197 Ω electrical resistance of $VO_2$ thin film. The thermal response time is that which is required to respond to a change in its ambient temperature:

$$T(t) = (T_2 - T_1)\left(1 - e^{-\frac{t}{\tau}}\right) + T_1 \tag{9}$$

where $T_1$ is the steady state temperature of the sensor, and $T_2$ is the ambient temperature. The extracted thermal response time is 14 μs.

As clarified by Eq. (3), the thermal resistance $R_{th}$ needs to be large enough for a high responsivity. However, the increase of $R_{th}$ leads to a rise of the thermal response time $\tau$. Therefore, there is a trade-off between the responsivity and $\tau$ in the design of the microbolometer. In order to have less impact on the thermal response time and maintaining a good thermal resistance, someone is able to further decrease the width of $VO_2$ thin film and the thickness of the buffer layer. However, the buffer layer should also be thick enough to provide robust mechanical support. We also note that further improvements to the responsivity is possible through vacuum packaging.

## 3.2 Electromagnetic behavior

The electromagnetic simulation is performed to analyze the impedance match and the received power of the antenna-coupled microbolometer operating in the transition region. The antenna was designed with a large air cutout and a 400 μm high ground plane, with the antenna and membrane supported by strategically etched 300-μm-thick Si substrate. The length and width of the dipole antenna were 2.28 mm and 0.6 mm, respectively. The antenna and the ground plane were modeled as perfect electric conductor

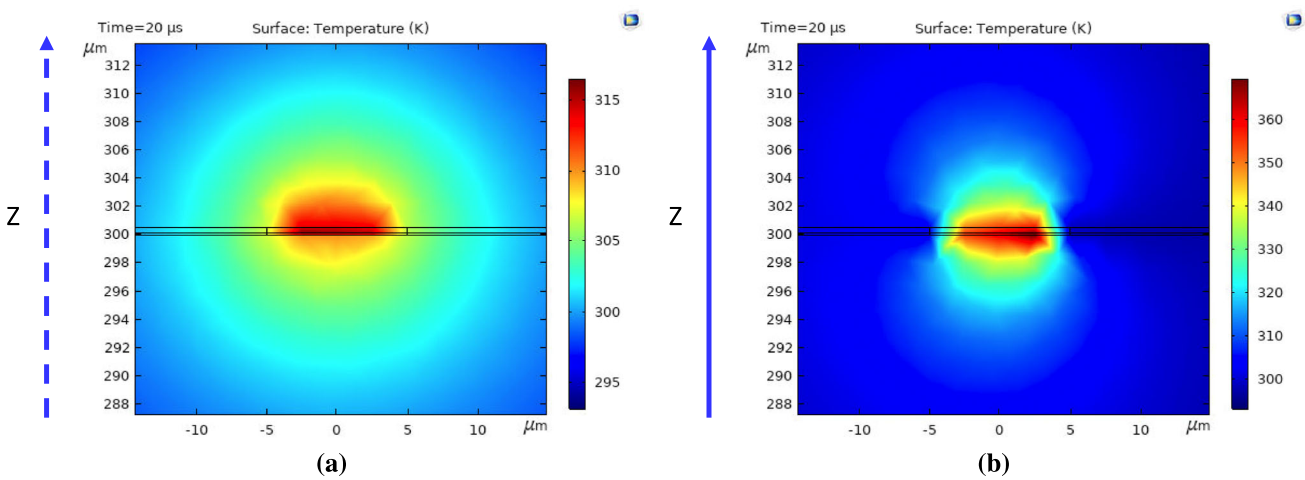


**Fig. 6** 2D cross-sectional temperature distribution across the sensor for **a** the on-substrate and **b** suspended designs

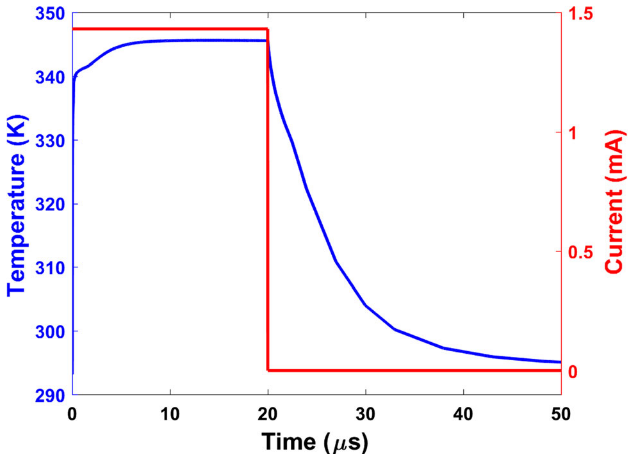


**Fig. 7** Dynamic response of the sensor with a current pulse (bias) of 1.43 mA

(PEC) and $VO_2$ was modeled as a lumped port. The PEC was used to simplify the modeling of the highly conductive gold and copper for a faster simulation. The return loss ($S_{11}$) and Smith chart for a single element with an impedance of 197 Ω are shown in Fig. 8. The antenna demonstrates a frequency range of $S_{11}$ operation at − 10 dB from 65 to 85 GHz and circles around the center of the Smith chart. The 2D radiation patterns with 5 GHz intervals from 66 to 81 GHz are presented in Fig. 9. The realized gain at the broadside is larger than 1.0 dB with antenna efficiency > 90.2%. To analyze the received power, background radiation is polarized to match the direction of the antenna. The received power at 75 GHz is approximately $1 \times 10^{-5}$ W with a 57 V/m E-field amplitude plane wave.

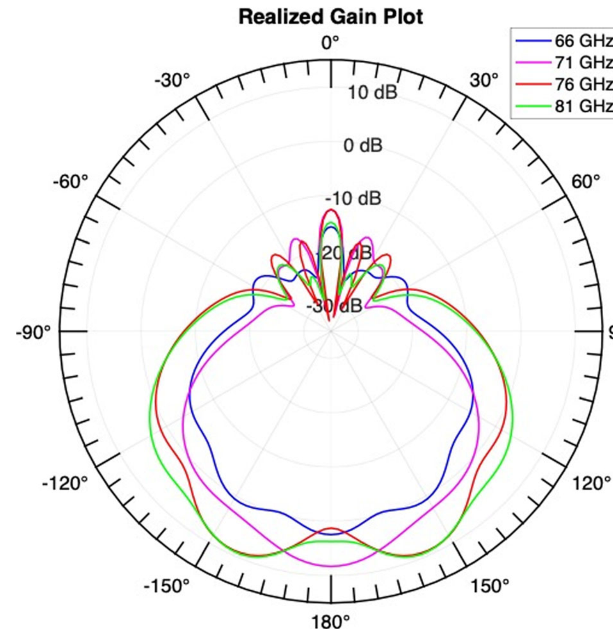


**Fig. 9** Magnitude of the realized gain from 66 to 81 GHz with 5 GHz intervals (y–z plane)

### 3.3 Responsivity and NEP

As described in Sect. 2.2, the performance of the proposed microbolometer is characterized by both the responsivity and NEP, which through the use of simulation results, are estimated by Eqs. (2), (4), respectively. The antenna-coupled microbolometer receives power from background radiation, leading to a temperature change that results in a resistance change. An additional boundary heat source is then applied at the top surface of $VO_2$ thin film. The other

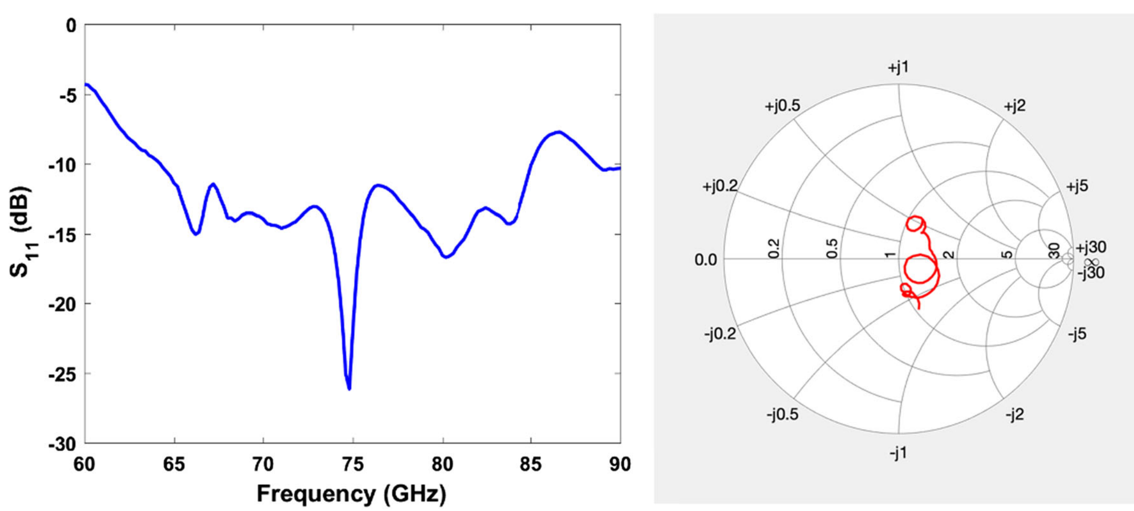


**Fig. 8** Simulated **a** $S_{11}$ return loss and **b** Smith chart of the $S_{11}$ for a single element showing that the antenna is impedance-matched from 65 to 85 GHz

**Table 2** Comparison of microbolometers

| | Antenna-coupled | Dimension ($\mu m^3$) | Responsivity (V/W) | NEP (pW/$\sqrt{}$Hz) |
|---|---|---|---|---|
| This work | Yes | 10 × 40 × 0.107 | 1.72 × $10^3$ | 33 |
| (Miller et al. 2004) | Yes | 10 × 1 × 0.035 | 85 | 25 |
| (Scheuring et al. 2013) | Yes | 2 × 5 × 0.07 | 33 | 152 |
| (Bevilacqua and Cherednichenko 2013) | Yes | 0.5 × 0.5 × 0.05 | 132 | 200 |
| (Tu et al. 2018) | No | 10 × 30 × 0.12 | 61.5 | 85 |

boundary condition settings are identical with that described in Sect. 3.1. When biasing the proposed suspended sensor at the phase transition cliff with the electrical resistance $R = 197\ \Omega$, the received power is around $1 \times 10^{-5}$ W with a 57 V/m E-field amplitude plane wave background radiation of 75 GHz. Then the electrical resistance decreases to 185 Ω and the antenna is also impedance-matched from 65 to 85 GHz. With an output voltage change of 17.2 mV, responsivity is extracted to about $1.72 \times 10^3$ V/W. Noise voltage sources are estimated by Eq. (5)-(8). Next, the $1/f$ noise voltage is negligible with a radiation modulation frequency $f = 100$ kHz. The large responsivity in the transition region results in a predominance of Phonon noise in the microbolometer. The approximate analytical NEP is 33 pW/$\sqrt{\text{Hz}}$, with $R = 197\ \Omega$ and $R_{th} = 6 \times 10^3$ K/W. Various bias current values were applied to the suspended sensor to test its operation at different temperatures caused by Joule heating. When applying a smaller bias current $I = 1.42$ mA, the electrical resistance increases to $R = 211\ \Omega$. The antenna is still impedance-matched from 65 to 85 GHz. Using the same analytical method described above, the responsivity and NEP are $1.70 \times 10^3$ V/W and 33 pW/$\sqrt{\text{Hz}}$, respectively. The slightly smaller responsivity compared with that biased at 1.43 mA is mainly due to a smaller bias current. With a larger bias current $I = 1.46$ mA, the electrical resistance is 152 Ω while the frequency range of the antenna decreases to 78–84 GHz. Together, the present findings show that a high responsivity ($10^3$ V/W) and a low NEP ($10^{-11}$ W/$\sqrt{\text{Hz}}$) can be achieved by biasing the proposed suspended sensor at the phase transition cliff with the electrical resistance $\sim$ 200 Ω where the antenna has a wideband operation. Compared to other designs, as shown in Table 2, the proposed architecture maintains a high responsivity and a low NEP. This new microbolometer design provides a path to achieve a passive uncooled mmW camera with hypersensitivity and relatively fast response. We also envision several challenges imposed by the hysteretic behavior of $VO_2$ due to complex non-linear effects, resulting in minor loop accommodation and stabilization issues with repetitive incoming radiation. One possible method to avoid this difficulty entails resetting the microbolometer after each radiation pulse by going all the way out of the hysteresis loop to the initial temperature (Gurvitch et al. 2010).

## 4 Conclusion

This paper presents a new design of high-performance (with orders of $10^3$ V/W responsivity and $10^{-11}$ W/$\sqrt{\text{Hz}}$ NEP) microbolometer for mmW imaging based on the non-linear behavior in the electrical resistivity of $VO_2$. The responsivity is significantly improved (> 10 times) by biasing the sensor near the phase transition region of $VO_2$ and the suspension using MEMS fabrication techniques. The temperature dependence of resistivity in our $VO_2$ thin films is measured and applied to the calculation of TCR, which is $\sim 10^3$ times larger in the phase transition region than the value of TCR in commonly used metals. Simulation results indicate a significant increase ($\sim 10^2$ times) in the thermal resistance by suspension as compared with on-substrate designs. The designed antenna exhibits a wideband impedance match from 65 to 85 GHz with a > 1.0 dB realized gain at broadside. A demonstrated enhancement to the responsivity ($1.72 \times 10^3$ V/W) of the proposed hypersensitive $VO_2$ microbolometer in turn yielded a low NEP (33 pW/$\sqrt{\text{Hz}}$). In the future, this new single pixel concept can be expanded into an array for mmW imaging applications at room temperature.

**Acknowledgements** This material is based upon work supported by the US National Science Foundation (NSF) CAREER Award under Grant No. 1845370 and the Air Force Research Lab (AFRL)/Defense Associated Graduate Student Innovators (DAGSI) Award No. RY6-OSU-19-2-AFRL2.

**Funding** The US National Science Foundation (NSF) CAREER Award under Grant No. 1845370 and the Air Force Research Lab (AFRL)/Defense Associated Graduate Student Innovators (DAGSI) Award No. RY6-OSU-19–2-AFRL2.

**Data availability** Not applicable.

**Code availability** Not applicable.

## Compliance with ethical standards

**Conflicts of interest** The authors declare that they have no competing interests.

## References


Appleby R, Anderton RN (2007) Millimeter-wave and submillimeter-wave imaging for security and surveillance. Proc IEEE 95:1683–1690. https://doi.org/10.1109/jproc.2007.898832

Berglund C, Guggenheim H (1969) Electronic properties of VO2 near the semiconductor-metal. Trans Phys Rev 185:1022

Bevilacqua S, Cherednichenko S (2013) Fast room temperature THz bolometers. In: 2013 38th international conference on infrared, millimeter, and Terahertz Waves (IRMMW-THz), 1–6 Sept 2013, pp 1–2. https://doi.org/10.1109/IRMMW-THz.2013.6665544

Chen X, Yi X (2005) VO2-based microbolometer uncooled infrared focal plane arrays with CMOS readout integrated circuit. In: Asia-Pacific optical communications, 2005. International Society for Optics and Photonics, pp 602032–602038

Chen C, Yi X, Zhao X, Xiong B (2001) Characterizations of VO2-based uncooled microbolometer linear array. Sens Actuators A 90:212–214. https://doi.org/10.1016/s0924-4247(01)00495-2

Chen S, Ghassemiparvin B, Ghalichechian N (2018) The design of high-responsivity millimeter wave imager using vanadium dioxide microbolometers. In: IET conference proceedings:201 (204 pp.)-201 (204 pp.)

Chen S, Lust M, Ghalichechian N (2019) A Vanadium dioxide microbolometer in the transition region for millimeter wave imaging. In: 2019 IEEE international symposium on antennas and propagation and USNC-URSI Radio Science Meeting, pp 1641–1642. https://doi.org/10.1109/APUSNCURSINRSM.2019.8888891

De Almeida L, Deep G, Lima A, Khrebtov I, Malyarov V, Neff H (2004) Modeling and performance of vanadium–oxide transition edge microbolometers. Appl Phys Lett 85:3605–3607

Denison DR, Knotts ME, McConney ME, Tsukruk VV (2009) Experimental characterization of mm-wave detection by a micro-array of golay cells. In: Passive millimeter-wave imaging technology XII, 2009. International Society for Optics and Photonics, p 73090J

Ghasr MT, Kharkovsky S, Bohnert R, Hirst B, Zoughi R (2013) 30 GHz linear high-resolution and rapid millimeter wave imaging system for NDE. IEEE Trans Antennas Propag 61:4733–4740. https://doi.org/10.1109/TAP.2013.2270174

Gurvitch M, Luryi S, Polyakov A, Shabalov A (2010) Treating the case of incurable hysteresis in VO2. In: Future trends in microelectronics: from nanophotonics to sensors and energy, pp 395–409

Hesler JL, Crowe TW (2007) Responsivity and noise measurements of zero-bias Schottky diode detectors. In: Proceedings of 18th international symposium on space terahertz technology, pp 89–92

Joung M et al (2004) Development of passive millimeter-wave imaging systems and its applications to medical- and bio-objects imaging. In: Terahertz for military and security applications II, Orlando, FL, 2004, pp 99–102

Kawakubo T, Nakagawa T (1964) Phase Transition in VO2. J Phys Soc Jpn 19:517–519. https://doi.org/10.1143/JPSJ.19.517

Lust M, Chen S, Wilson CE, Argo J, Doan-Nguyen V, Ghalichechian N (2020) High-contrast, highly textured VO2 thin films integrated on silicon substrates using annealed Al2O3 buffer layers. J Appl Phys 127:205303. https://doi.org/10.1063/1.5144816

Miller AJ, Luukanen A, Grossman EN (2004) Micromachined antenna-coupled uncooled microbolometers for terahertz imaging arrays. In: Terahertz for military and security applications II, Orlando, FL, 2004, pp 18–24

Neikirk D, Lam WW, Rutledge D (1984) Far-infrared microbolometer detectors. Int J Infrared Millimeter Waves 5:245–278

Neto G, de Almeida LAL, Lima AMN, Moreira CS, Neff H, Khrebtov IA, Malyarov VG (2008) Figures of merit and optimization of a VO2 microbolometer with strong electrothermal feedback. Opt Eng 47:073603–073615. https://doi.org/10.1117/1.2956386

Ordonez-Miranda J, Ezzahri Y, Joulain K, Drevillon J, Alvarado-Gil JJ (2018) Modeling of the electrical conductivity, thermal conductivity, and specific heat capacity of VO2. Phys Rev B 98:075144. https://doi.org/10.1103/PhysRevB.98.075144

Reintsema CD, Grossman EN, Koch JA (1999) Improved VO2 microbolometers for infrared imaging: operation on the semiconducting-metallic phase transition with negative electrothermal feedback. In: Infrared technology and applications XXV, 1999. International Society for Optics and Photonics, pp 190–201

Scheuring A, Thoma P, Day J, Il'in K, Hanisch J, Holzapfel B, Siegel M (2013) Thin Pr–Ba–Cu–O Film Antenna-Coupled THz Bolometers for Room Temperature Operation. IEEE Trans Terahertz Sci Technol 3:103–109. https://doi.org/10.1109/TTHZ.2012.2226880

Schuetz CA, Samluk J, Chen C, Prather DW (2007) Millimeter-wave imaging using optical upconversion detectors. In: Electro-Optical remote sensing, detection, and photonic technologies and their applications, 2007. International Society for Optics and Photonics, p 67390R

Son LN, Tachiki T, Uchida T (2013) Fabrication and evaluation of thin-film spiral-antenna-coupled VOx microbolometer by metal-organic decomposition. Jpn J Appl Phys 52:046601. https://doi.org/10.7567/jjap.52.046601

Tiwari A, Satoh H, Aoki M, Takeda M, Hiromoto N, Inokawa H (2015) Fabrication and analytical modeling of integrated heater and thermistor for antenna-coupled bolometers. Sens Actuators A 222:160–166. https://doi.org/10.1016/j.sna.2014.10.003

Tu X et al (2018) Nb5N6 microbolometer for sensitive, fast-response, 2-μm detection. Opt Express 26:15585–15593

Wang B, Lai J, Li H, Hu H, Chen S (2013) Nanostructured vanadium oxide thin film with high TCR at room temperature for microbolometer. Infrared Phys Technol 57:8–13

Yang F, Wang Z, Dou W, Sun Z (2015) Zero-biased diode Schottky detector for low cost preamplified millimeter-wave imaging. Microwave Opt Technol Lett 57:2690–2693. https://doi.org/10.1002/mop.29420

Yang H-H, Rebeiz GM (2015) Micromachined room-temperature air-suspended Ni/Cr nanobolometer. IEEE Trans Microw Theory Tech 63:3760–3767

Yoneoka S et al (2011) ALD-metal uncooled bolometer. In: 2011 IEEE 24th international conference on micro electro mechanical systems, 23–27 January 2011, pp 676–679. https://doi.org/10.1109/MEMSYS.2011.5734515

Zerov VY, Kulikov YV, Leonov V, Malyarov V, Khrebtov I, Shaganov I (1999) Features of the operation of a bolometer based on a vanadium dioxide film in a temperature interval that includes a phase transition. J Opt Technol 66:387